

Pyrene-Based Self-Assembled Monolayer with Improved Surface Coverage and Energy Level Alignment for Perovskite Solar Cells

Peer-reviewed author version

LENAERS, Stijn; LAMMAR, Stijn; KRISHNA, Anurag; Stacchini, Valerio; CARDEYNAELS, Tom; PENXTEN, Huguette; Weijters, Christ; Verhage, Michael; RUTTENS, Bart; MAES, Wouter; D'HAEN, Jan; Musiienko, Artem; AERNOUTS, Tom; LUTSEN, Laurence; VANDERZANDE, Dirk; POORTMANS, Jef & VAN GOMPEL, Wouter (2024) Pyrene-Based Self-Assembled Monolayer with Improved Surface Coverage and Energy Level Alignment for Perovskite Solar Cells. In: *Advanced functional materials*,.

DOI: 10.1002/adfm.202411922

Handle: <http://hdl.handle.net/1942/44694>

Pyrene-based self-assembled monolayer with improved surface coverage and energy level alignment for perovskite solar cells

Stijn Lenaers ^a, Stijn Lammar ^{a,b,c,d}, Anurag Krishna ^{a,c,d}, Valerio Stacchini ^e, Tom Cardeynaels ^a, Huguette Penxten ^a, Christ Weijtens ^f, Michael Verhage ^{f,g}, Bart Ruttens ^a, Wouter Maes ^{a,d}, Jan D'Haen ^a, Artem Musiienko ^e, Tom Aernouts ^{a,c,d}, Laurence Lutsen ^{a,d}, Dirk Vanderzande ^{a,d}, Jef Poortmans ^{a,b,c,d} and Wouter Van Gompel ^a

^aHasselt University, imo-imomec, Martelarenlaan 42, 3500 Hasselt, Belgium

^bDepartment of Electrical Engineering (ESAT), Katholieke Universiteit Leuven, Kasteelpark Arenberg 10, 3001 Leuven, Belgium

^cimec, imo-imomec, Thin Film PV Technology – partner in Solliance, Thor Park 8320, 3600 Genk, Belgium

^dEnergyVille, imo-imomec, Thor Park 8320, 3600 Genk, Belgium

^eHelmholtz-Zentrum Berlin, Albert-Einstein-Straße 16, 12489 Berlin, Germany

^fDepartment of Applied Physics and Science Education, Eindhoven University of Technology, P.O. Box 513, 5600 MB Eindhoven, The Netherlands

^gMolecular Materials and Nanosystems, Institute for Complex Molecular Systems, Eindhoven University of Technology, Partner in Solliance, P.O. Box 513, 5600 MB Eindhoven, The Netherlands.

Keywords: perovskite solar cells, Self-assembled monolayer, surface coverage, energy level alignment

Abstract

Recently, the efficiency of *p-i-n* perovskite solar cells drastically increased, a pivotal factor being the incorporation of self-assembled monolayers (SAMs) as hole-transporting layer (HTL). SAMs offer many advantages over conventional HTLs, including minimal material requirements, low cost, and facile processing. Current research is mainly focused on the development of carbazole-derived SAMs. However, the versatility of organic chemistry allows for the design of SAMs with alternative organic cores that may possess specific benefits. In this study, three novel SAMs are incorporated in *p-i-n* perovskite solar cells, each based on an aromatic core commonly used in organic semiconductors. The novel SAMs vary in their energy level alignment with the perovskite active layer. Optimal alignment is achieved with a pyrene-based SAM (4PAPyr), resulting in solar cells which outperform the commercially available 2PACz. Moreover, due to improved surface coverage, the use of 4PAPyr leads to a significantly higher number of working solar cell devices when compared to 2PACz, which is of particular interest with regard to upscaling. After device optimization, a power conversion efficiency of

22.2% was achieved with 4PAPyr. This research underlines the importance of diversifying SAMs to unlock further advancements in perovskite solar cell efficiency and scalability.

Introduction

Over the past couple of years, perovskite solar cells (PSCs) have developed at a rapid pace, increasing from a power conversion efficiency (PCE) of 3.8% in 2009 to an astounding 26.1% in 2023.^[1] While, nowadays, high efficiencies can be achieved for solar cell devices with the regular (*n-i-p*) as well as the inverted (*p-i-n*) device configuration, the efficiency of *p-i-n* PSCs still lags behind.^[2] Despite this, inverted *p-i-n* PSCs have recently sparked increasing interest due to the many advantages they offer over their *n-i-p* counterparts. More specifically, these include higher device stability, no need for the use of dopants for the hole-transporting layer (HTL) that can cause degradation, improved low-temperature processability, low current-voltage hysteresis, and better compatibility with perovskite-based tandem solar cells.^[3]

The main reason for the lower PCE of inverted solar cells is the increase of voltage losses due to charge recombination at the interfaces between the perovskite and the charge transporting layers (CTLs), with most of the losses occurring at the interface with the hole transporting layer.^[4] To minimize these losses, hole-transporting materials that form energetically well-aligned interfaces with the perovskite layer are required, resulting in efficient hole extraction and preventing undesirable charge recombination. Most HTL materials can be divided into one of two groups: 1) conjugated polymers, such as poly[bis(4-phenyl)(2,4,6-trimethylphenyl)amine] (PTAA)^[5], and 2) inorganic semiconductors, such as nickel oxide (NiO_x).^[6] While PTAA offers the advantage of low-temperature solution processing, it also results in poor surface wettability and degrades when exposed to high temperatures.^[7] NiO_x, on the other hand, can easily be applied on a large scale by sputtering techniques, but also requires additional treatment steps such as thermal annealing.^[8] Additionally, NiO_x can act as both a Brønsted proton acceptor and a Lewis electron acceptor, deprotonating cationic amines and oxidizing iodide species.^[8] This results in the formation of hole extraction barriers at the perovskite-NiO_x interface.

It is thus clear that apart from these conventional HTLs, other types of transport layers need to be developed to facilitate large-scale production of PSCs. A promising alternative type of materials are self-assembled monolayers (SAMs)^[9], offering the advantages of manifold substrate compatibility,^[10] potential low cost^[11], and facile processing through a variety of techniques including spin-coating^[12], dip-coating^[13], spray-coating^[14] or, evaporation^[15], while only requiring a minimal amount of material. Additionally, proper energy level alignment can be ensured by finetuning the molecular structure of the SAM.^[16] The first SAMs that could compete with the conventional HTLs in perovskite solar cells were the carbazole-based phosphonic acids (PA) **2PACz** ([2-(9*H*-carbazol-9-yl)ethyl]phosphonic acid) and **MeO-2PACz** ([2-(3,6-dimethoxy-9*H*-carbazol-9-yl)ethyl]phosphonic acid)), developed by Al-Ashouri *et al.* in 2019.^[17] This sparked a surge in the research on SAMs as HTLs in *p-i-n* perovskite solar cells. Despite the vast quantity of research conducted on these self-assembled monolayers in recent years, the majority of efforts concentrate on SAMs with a similar molecular structure. Typically, the organic core of the SAM consists of carbazole derivatives^[12, 18] or carbazole-like molecules such as phenothiazine.^[19] While these carbazole-derived SAMs have proven their

effectiveness as HTLs in PSCs, they still face several drawbacks, such as poor wettability when applied directly on the ITO electrode, resulting in a low percentage of working devices.^[13, 20] While the yield of working devices can be improved by combining SAMs with the conventional HTL NiO_x^[10b], and additives such as potassium fluoride (KF) can improve the long-term stability and hole conductivity^[21], these additional layers also greatly increase the device complexity. In contrast, research into alternative organic cores for phosphonic acid SAMs to be used as HTL in PSCs without these drawbacks is limited.^[22] As a result, the influence of the organic core on the functioning of the phosphonic acid SAM as HTL is poorly understood.

To gain more insights into the importance of the molecular structure of the organic core of the SAM, we developed three novel SAMs that are based on three organic cores commonly employed in organic semiconductors: pyrene (Pyr), naphthalene (Naph), and benzothienobenzothiophene (BTBT) (Figure 1a-c). The choice for the polycyclic aromatic pyrene core was inspired by earlier work on a pyrene-derived organic ammonium cation for the formation of a 2D perovskite.^[23] With the pyrene core tethered to the inorganic framework via an alkylammonium tail, the pyrene ammonium salt formed a densely packed and highly ordered organic layer. Although the packing of a pyrene phosphonic acid on a surface will surely differ from that of an organic cation inside a 2D perovskite, the propensity of tethered pyrene cores to form a highly ordered layer served as our rationale for the choice of this core. The smaller bicyclic aromatic naphthalene moiety was chosen for comparison with pyrene. The resulting phosphonic acid (PA) SAMs are **4PAPyr** ([4-(pyren-1-yl)butyl]phosphonic acid) and **2PANaph** ([2-(naphthalen-2-yl)ethyl]phosphonic acid). Finally, the BTBT core was selected because of its high hole mobility, resulting in the SAM **3PABTBT** ([3-(benzo[*b*]benzo[4,5]thieno[2,3-*d*]thiophen-2-yl)propyl]phosphonic acid).^[24] In our previous work, we already showed that an ammonium iodide salt with a BTBT organic core outperforms its carbazole counterpart as a bottom interlayer in *p-i-n* solar cells.^[25] Furthermore, it was also shown that the same BTBT ammonium iodide salt can increase the stability of both perovskite solar cells and the black phase of cesium lead iodide in photodetectors.^[25-26] Additionally, the three novel SAMs will exhibit different electronic properties, enabling us to investigate the impact of energy level alignment between the perovskite and SAM on the overall device performance. The newly synthesized SAMs were incorporated in triple cation (3C) *p-i-n* perovskite solar cells and compared with the commercially available SAM **2PACz**. The resulting device data clearly showed that **4PAPyr** outperforms all other SAMs, including **2PACz**, in terms of power conversion efficiency. With the same device configuration, the champion PCE was increased from 18.4% for **2PACz** to 20.2% with **4PAPyr**. Transient photovoltage measurements confirm that **4PAPyr** outperforms **2PACz** in terms of selective hole extraction. Additionally, the coverage of the **4PAPyr** SAM on ITO is superior to that of **2PACz**, resulting in a much smaller spread in open-circuit voltage (V_{oc}) over multiple devices. With further dedicated device optimization, devices with **4PAPyr** reached a maximum PCE of up to 22.2%. Furthermore, the devices with **4PAPyr** showed reduced current-voltage hysteresis and enhanced stability under maximum power-point tracking (MPPT) as compared to devices with **2PACz**. During 180 hours of continuous MPPT devices with **4PAPyr** maintained 93% of the initial efficiency after a burn-in period of 16 hours.^[27] Meanwhile, devices with **2PACz** only maintained 74% of their initial efficiency during

the same time period. Note that our novel pyrene-based phosphonic acid **4PAPyr** possesses a different alkyl chain length as compared to the **2PACz** reference. It has been shown in the literature that each organic core may possess a different optimal chain length for its functionality as a SAM in a perovskite solar cell. For example, for phosphonic acids with a carbazole core (PACz) it has been shown that **2PACz** with a chain length of 2 carbons is superior to **4PACz** with a chain length of 4 carbons, while for phosphonic acids with a methylated carbazole core (Me-PACz) the opposite is true and **Me-4PACz** is superior to **Me-2PACz**.^[12, 28] Based on the greater bulkiness of the pyrene core (Pyr) as compared to the carbazole core (Cz), we tentatively hypothesized that a chain length of 4 carbon atoms could be more suitable. Since **4PAPyr** possesses superior characteristics in terms of coverage and the stability and efficiency of the resulting solar cells as compared to the reference **2PACz**, we suggest that a dedicated chain length optimization study of phosphonic acids with a pyrene core is worthwhile.

Results and Discussion

For the synthesis of the phosphonic acids (Figure 1 d), the functionalization of the aromatic cores with an alkyl chain containing a halogen end group is required. For **3PABTBT**, this product was obtained through a Friedel-Crafts acylation followed by a reduction reaction. The brominated precursors of **4PAPyr** and **2PANaph** were synthesized through a reduction of the commercially available carboxylic acid starting materials into alcohols, followed by an Appel substitution reaction. All of these brominated compounds were subsequently converted into the desired PAs via the same two-step synthesis pathway (Figure 1d).^[12] Details on the synthesis can be found in the supporting information.

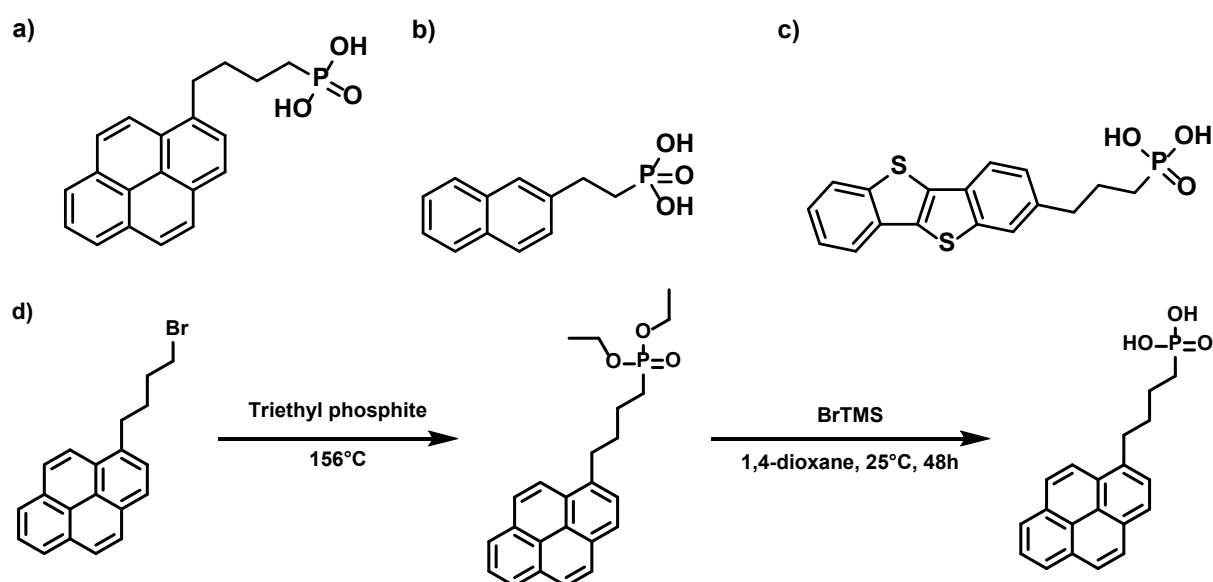


Figure 1: Molecular structure of the three newly synthesized PAs: a) [3-(benzo[b]benzo[4,5]thieno[2,3-d]thiophen-2-yl)propyl]phosphonic acid, b) [4-(pyren-1-yl)butyl]phosphonic acid, c) [2-(naphthalen-2-yl)ethyl]phosphonic acid, and d) schematic representation of the general synthetic route of the PAs (BrTMS = bromotrimethylsilane).

The highest occupied molecular orbital (HOMO) energy level of each PA was determined in three different ways: 1) theoretically via density functional theory (DFT) calculations, 2) experimentally by cyclic voltammetry (CV), and 3) ultraviolet photoelectron spectroscopy

(UPS). The results are summarized in Table 1. While there are slight variations in absolute values between the three methods, there is a clear overall trend in which **4PAPyr** has the highest HOMO of around -5.5 eV, followed by **2PACz** with a HOMO that is closer to -5.7 eV. The other two PAs have HOMO values that are deeper than that of the **2PACz** reference, with values of -5.75 eV and -6.1 eV respectively for **3PABTBT** and **2PANaph**. When comparing the HOMO level relative to the Fermi level (ionization potential (IP) – work function (WF)), as determined via UPS, a similar trend can be seen as when comparing them to the vacuum level. The HOMO level of **4PAPyr** is slightly closer to the Fermi level than that for the reference **2PACz** and the other two newly synthesized PAs possess slightly higher differences between the Fermi- and HOMO level.

Table 1: HOMO energy levels of the newly synthesized PAs and the reference material, 2PACz, as determined using cyclic voltammetry (CV), density functional theory (DFT), and ultraviolet photoelectron spectroscopy (UPS). The Fermi level (IP-WF) was calculated by subtracting the work function from the ionization potential, both obtained via UPS.

SAM	HOMO (eV) CV	HOMO (eV) DFT	HOMO (eV) UPS	$E_F - \text{HOMO}$ (eV) UPS
4PAPyr	-5.59	-5.53	-5.49	0.81
2PACz	-5.64	-5.79	-5.78	0.87
3PABTBT	-5.74	-5.82	-5.72	1.16
2PANaph	-5.75	-6.12	-6.14	1.53

UPS measurements on the perovskite active layer

By comparing the obtained HOMO levels of the SAMs with the valence band maximum (VBM) of the triple-cation perovskite that we utilized ($\text{Cs}_{0.05}\text{FA}_{0.85}\text{MA}_{0.10}\text{Pb}(\text{I}_{0.90}\text{Br}_{0.10})_3$), an estimation can be made as to which molecules will be most suited as hole transporting materials, since a HOMO level that is slightly higher than the VBM of the perovskite material is required for optimal hole extraction. For the past few decades, UPS has been the preferred technique for determining the VBM of semiconductors. In these measurements, it is commonly assumed that the VBM can be extracted by using a linear extrapolation to the background level of the leading edge of the UPS valence band spectrum.^[29] In recent years, it was however pointed out that this way of extracting the VBM from UPS spectra is not suitable for hybrid perovskites, due to an intrinsically low density of states (DOS) at the top of the valence band, resulting in a systematic overestimation of the ionization potential (IP) when employing such a linear extrapolation.^[30] Therefore, we employed the methodology described by Endres *et al.*^[31], where the spectrum is plotted on a logarithmic scale and the VBM is determined via linear extrapolation of the leading edge of the valence band spectrum (see the SI for a more detailed discussion of the method).

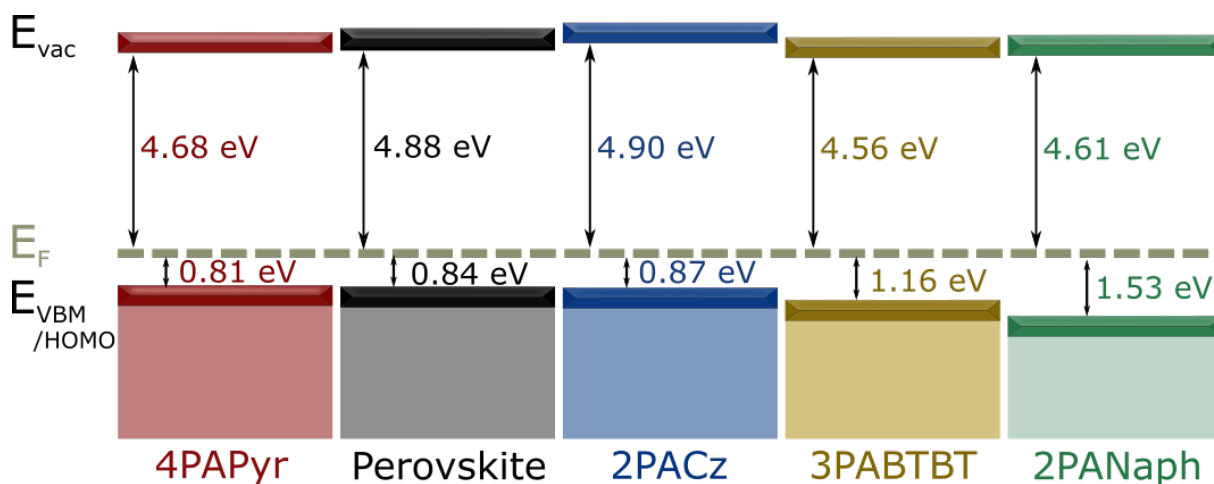


Figure 2: Schematic representation of the HOMO levels and valence band maximum of the SAMs and perovskite ($CS_{0.05}FA_{0.85}MA_{0.10}Pb(I_{0.90}Br_{0.10})_3$) with respect to their corresponding Fermi levels (E_F).

Figure 2 shows the HOMO levels of the newly synthesized SAMs and the **2PACz** reference compared to the VBM of the perovskite used in our device stack obtained via UPS measurement. All given values are with respect to the Fermi level (E_F). This comparison is of particular interest as it gives the closest resemblance to the actual situation inside the devices, in which the Fermi levels of different semiconductors tend to align (at equilibrium in the dark). The HOMO levels for **4PAPyr** and **2PACz** are located close to the VBM of the perovskite and have a similar difference between the HOMO and the Fermi level (Table 1). This allows for a favourable energy level alignment with the perovskite, which should promote efficient hole extraction. In the case of **3PABTBT** and **2PANaph**, the opposite is true, which results in poor energy level alignment, possibly creating an energy barrier that impedes efficient hole extraction.

It needs to be taken into consideration that the HOMO values for all SAMs are determined without considering possible effects from interactions with the perovskite layer which could have an influence on the orientation of the molecules inside the SAM. The HOMO level of pyrenyl-containing molecules, for example, is known to be sensitive to the molecular orientation of the pyrenyl core and to interactions with metal ions.^[32] Hence, interactions with the lead ions of the perovskite and changes in the orientation of the pyrenyl core in the SAM can influence the energy level alignment with the perovskite in the final device. Nonetheless, the determined energy level alignment correlates well with the device characteristics.

Devices with an NiO_x HTL

To assess their potential as effective HTL materials, the four different SAMs were initially employed at the NiO_x/perovskite interface as shown in Fig. 3. Although the carbazole-based SAMs were originally designed to be used at the ITO/perovskite interface^[33], we note that the yield of such devices (i.e. the percentage of properly functioning devices) can be rather low depending on the coverage of the SAMs (*vide infra*). This issue has also been reported in the literature, in which poor coverage of SAMs on ITO causes severe shunting of the PSCs due to direct contact between ITO and the perovskite layer.^[10b, 34] For this purpose, an NiO_x layer is often used on top of ITO. The NiO_x layer can act as a “safety net” against shunting, since it is a HTL material, while providing similar binding sites for the SAM as ITO.^[10b, 34] Furthermore, it

has been shown that the higher reactivity of NiO_x compared to ITO causes stronger binding with the SAM molecules, resulting in a more uniform coverage. Although the use of NiO_x typically results in a slightly inferior device performance due to higher series resistance, it provides a more reliable basis for comparing the performance of the four SAMs as a HTL without initially needing to consider potential differences in surface coverage that would be critical when depositing on bare ITO. The corresponding J-V curves are shown in Fig. 3a. One of the new SAMs, namely **4PAPyr** demonstrates promising results, showing an improved device performance compared to **2PACz**, which serves as the control in this study. The other two novel SAMs result in the formation of an s-shape feature in the J-V curve, pointing to the formation of an energy barrier at the interface that impedes effective hole extraction.^[35] Indeed, the UPS and CV measurements discussed above already suggested that **4PAPyr** and **2PACz** were most likely to achieve good energy level alignments with our perovskite material. Furthermore, the s-shape seems to worsen with the deeper HOMO levels and increasing difference between the E_F and the HOMO of the other two SAMs, which should result in an increasing energy barrier.^[35]

We do not notice any significant effects of the nature of the SAM on the grain size of the perovskite film. Figure S11 shows SEM images of the perovskite deposited on top of the different SAMs. All images show a great similarity, indicating that there are no major differences in grain size between the perovskite films deposited on the different SAMs. The bright white crystallites on top of the perovskite films, as apparent in the SEM images, are expected to be lead iodide crystallites.^[36] The formation of lead iodide crystallites at the surface of solution-processed perovskite films with a similar composition has been shown before in the literature.^[37] Furthermore, we used the Scherrer equation to obtain a rough estimate of the crystallite size from the XRD patterns of the perovskite film on bare ITO, 4PAPyr, and 2PACz (Figure S10). The first reflection corresponding to the perovskite phase at ~14° 2θ was fitted using the Pearson-VII function to extract the FWHM, resulting in the following crystallite size according to Scherrer (using a Scherrer constant, K, of 0.98): Bare ITO: 48.8 nm, 2PACz: 50.1 nm, and 4PAPyr: 51.4 nm. The obtained crystallite sizes are very similar, indicating that the SAMs do not have a significant influence on the crystallite size of the perovskite thin film in our study.

Given the promising results with **4PAPyr**, we focus on this SAM for the remainder of the study, with **2PACz** serving as the reference.

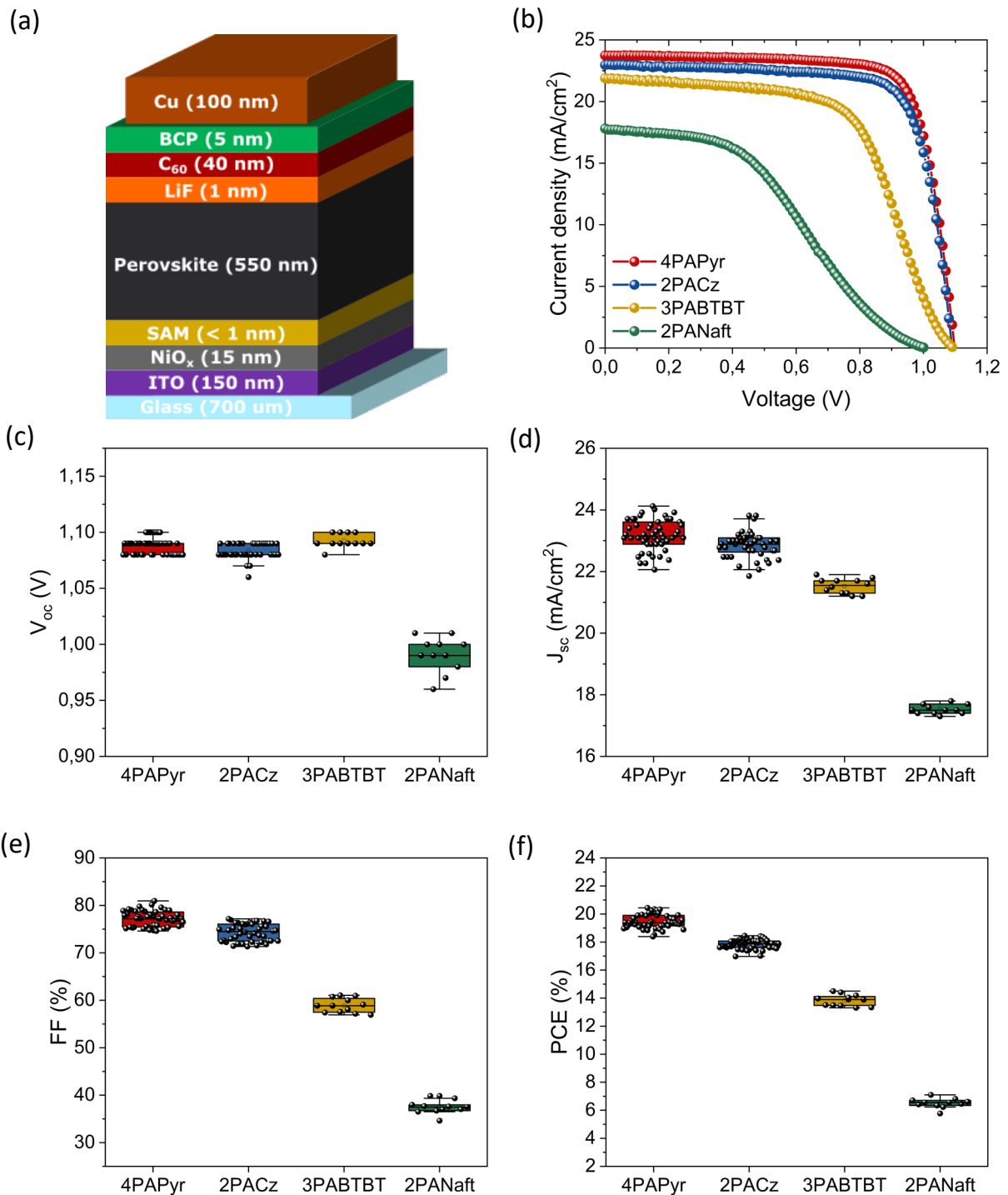


Figure 3: a) Schematic depiction of the device stack featuring the NiO_x-SAM bilayer. b-f) Performance results of devices including the different SAMs, showcasing J-V curves alongside the key metrics: open-circuit voltage (V_{oc}), current density (J_{sc}), fill factor (FF), and overall cell efficiency (PCE).

Devices without an NiO_x HTL

To simplify the device stack and to examine possible differences in coverage between **2PACz** and **4PAPyr**, the SAMs were directly applied on top of ITO. Over 70 devices were fabricated for both SAMs to ensure proper device statistics. As mentioned earlier, poor coverage of the

SAM will result in (severe) shunting of the device given the absence of NiO_x. Consequently, the V_{oc} of such shunted devices will be significantly lower.

The corresponding J-V data are displayed in Fig. 4. The smaller spread of the V_{oc} for ITO/4PAPyr in Fig. 4b indicates that **4PAPyr** results in a better overall coverage, which is in line with our hypothesis that the use of pyrene as an organic core for SAMs may lead to the formation of a highly ordered (mono)layer. The notably enhanced reproducibility of devices prepared using **4PAPyr** on ITO, in contrast to those with **2PACz**, is highly encouraging, especially given the straightforward processing approach used in our study, which consisted of simply spin coating the SAMs on top of ITO. Fast and facile deposition of the SAM is beneficial for scaling up solar cell production. Other approaches for the deposition of phosphonic acid SAMs on ITO that require more dedicated process optimization such as dip coating^[13], evaporation^[15], or using the SAM directly in the perovskite precursor^[38] may further improve the yield of the devices, but are beyond the scope of the current study. Next to improved reproducibility, superior performance was achieved also with **4PAPyr**, with a champion PCE of 20.2% (22.6 mA/cm², 1.11V, 80.4%) compared to 18.4% (21.7 mA/cm², 1.08V, 78.4%) for **2PACz**. Furthermore, the devices with **4PAPyr** showcased three additional benefits over devices with **2PACz**. Firstly, the current-voltage hysteresis is substantially reduced with **4PAPyr** (Table 2). The hysteresis index (HI) is calculated as:

$$HI = 100 \times \frac{PCE(reverse) - PCE(forward)}{PCE(reverse)}$$

Secondly, the devices with **4PAPyr** were significantly more stable during light soaking. The light-soaking effect (LSE) is a well-known phenomenon employed to enhance the V_{oc} of PSCs by illuminating the cells held under open-circuit conditions.^[39] In between subsequent J-V measurements, cells are held under such conditions for roughly one minute. As shown in Fig. 4e-f, it required 13 measurements (around 15 minutes) to achieve maximum performance with **2PACz**, whereas only 2 measurements (around 3 minutes) were needed for **4PAPyr**. This indicates that the devices with 4PAPyr reach equilibrium conditions faster under these conditions. Thirdly, the maximum power-point tracking (MPPT) output remained more stable for **4PAPyr**, as illustrated in Fig. 4d. These three benefits could potentially originate from suppressed effects of ion migration in the devices. Ion migration has been widely accepted as the origin of hysteresis in PSCs^[40], and recent reports are also suggesting it to be an important contributing factor towards the LSE^[34d, 41]. According to these reports, the mobile ions accumulate at the perovskite/CTL interfaces in the dark due to the built-in voltage, V_{bi}, in the devices. Upon illumination, at open-circuit conditions, the photovoltage initiates a redistribution of the mobile ions, resulting in an increasing V_{oc}. Herterich *et. al.* show by drift-diffusion simulations that a larger concentration of mobile ions will lead to a lower initial V_{oc}, and, therefore, a longer stabilization time for the V_{oc} under light-soaking, which has the same maximum value regardless of the ion concentration.^[41c] This is also shown experimentally by Biao *et. al.*, where incorporation of Cs⁺ in their FAMA perovskite resulted in a lower density of mobile ions and a suppressed LSE.^[34d] During MPPT conditions, there is a larger electric field across the perovskite layer compared to the open-circuit condition, causing the ions to slowly accumulate again at the interfaces, resulting in a declining V_{MPP} (i.e., the opposite effect of

LSE) and therefore a reduced MPPT output.^[41c] Since there are no clear differences in the crystallization of the perovskite on top of the two SAMs based on XRD and SEM measurements (Figures S10 and S11 in the SI), our tentative hypothesis is that the difference in stabilization time under light-soaking, as well as the more stable MPPT behaviour, is related to a lower defect density at the **4PAPyr**/perovskite interface.

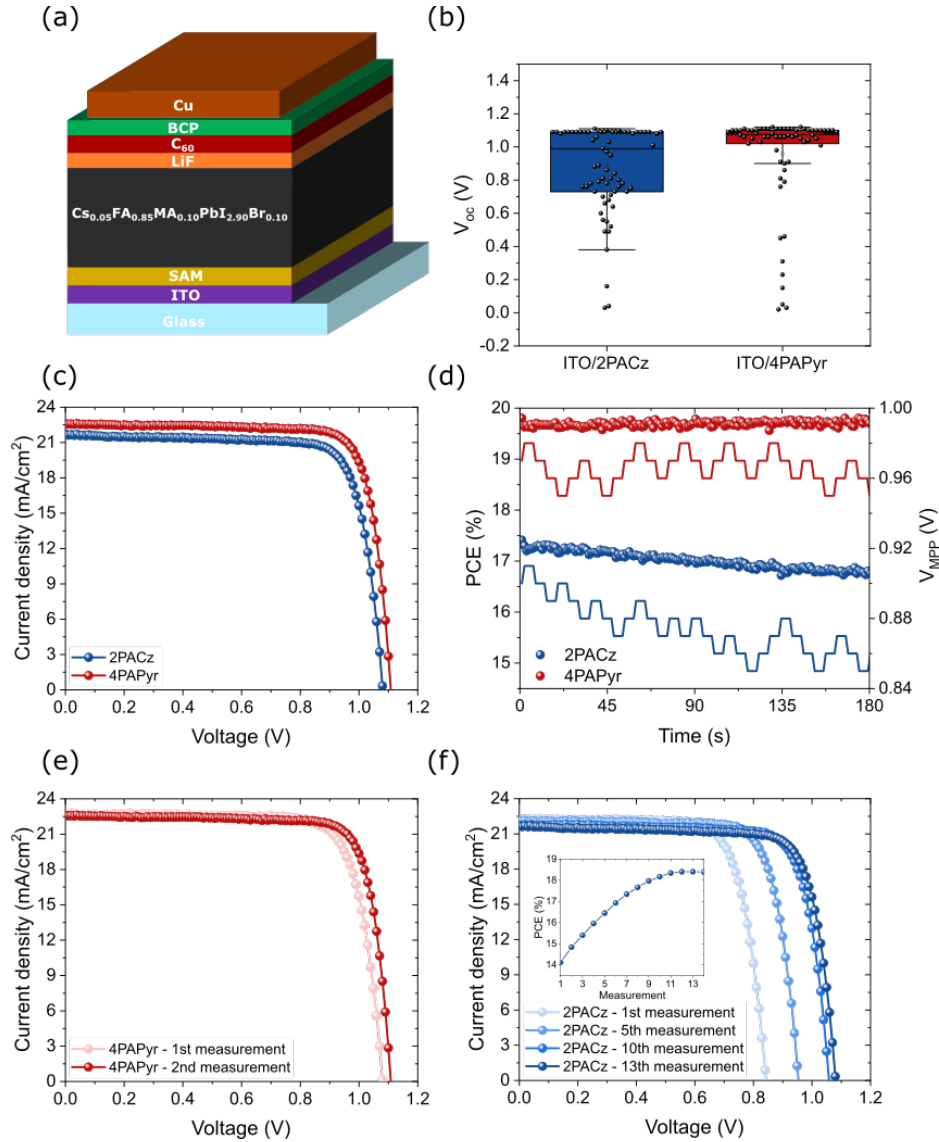


Figure 4: a) Schematic depiction of device stack with SAMs directly on top of ITO, b) difference in V_{oc} spread between 2PACz and 4PAPyr, showcasing the effect of overall better coverage for 4PAPyr, c) J-V curves of 4PAPyr and 2PACz directly on ITO, d) Max Power Point Tracking (MPPT) output of devices with both SAMs over time, e-f) difference in Light soaking effect between 4PAPyr and 2PACz respectively.

Table 2: Reverse and forward scan data of the champion devices of both 2PACz and 4PAPyr.

SAM	Direction	J _{sc} [mA/cm ²]	V _{oc} [V]	FF [%]	PCE [%]	HI
2PACz	Reverse	21.2	1.09	77.2	17.9	7.7
	Forward	21.2	1.06	73.5	16.5	
4PAPyr	Reverse	22.3	1.11	80.3	19.9	4.6
	Forward	22.4	1.11	76.3	18.9	

The maximum power point of devices with **4PAPyr** and **2PACz** was also tracked over an extended period of time under an elevated temperature of 65°C and 1 sun illumination (full spectrum and no UV filter; Figure 5). During the initial phase of the stability measurements a clear drop in efficiency for both SAMs can be observed. This initial rapid decline of efficiency or “burn-in time” is known in literature^[27, 42] and significantly influences the early performance of solar cells, usually resulting in losses of around 25% of the initial efficiency.^[43] In our case the device with **4PAPyr** lost 23% of its initial efficiency during the burn-in period of 16 hours, compared to **2PACz** who lost 39% of its initial efficiency during the same period. After this initial drop both samples were measured for an additional 180 hours during which the **4PAPyr** sample maintained 93% of its remaining efficiency and the sample with **2PACz** only 74%. Thus clearly showing that the novel SAM **4PAPyr** is significantly more stable than **2PACz** both during the initial burn-in period and long-term.

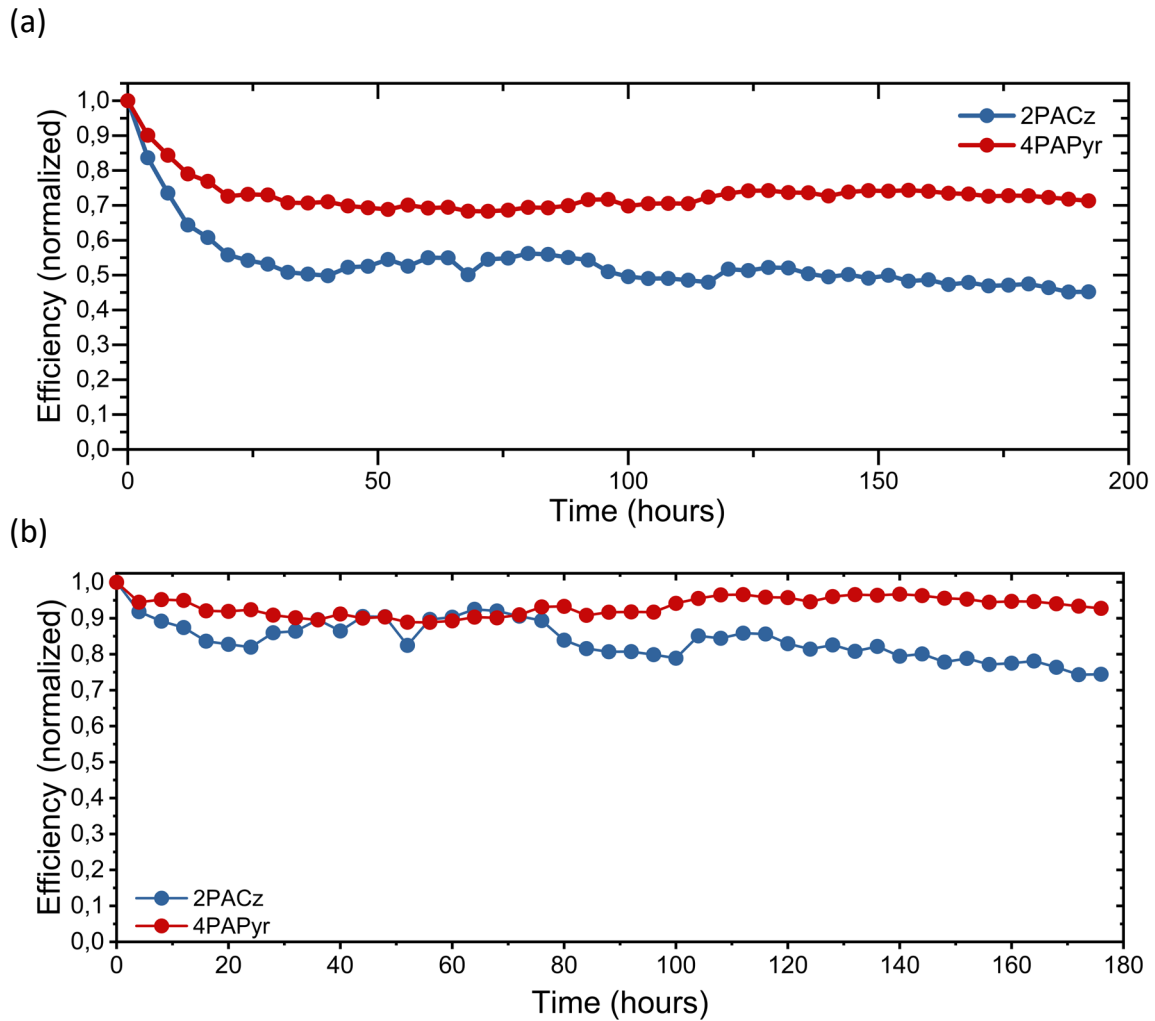


Figure 5: a) Maximum power point (MPP) tracking of devices with 4PAPyr and 2PACz under continuous 1-sun light soaking at 65°C. b) MPP tracking of devices with 4PAPyr and 2PACz without the initial burn-in period of 16 hours.

To further maximize the efficiency of the devices with **4PAPyr**, methyl ammonium chloride (MACl) was used as an additive in the perovskite precursor solution and MgF_2 was added to the device stack as an anti-reflective coating (ARC), as illustrated in Fig. 6. MACl is a widely used additive to improve the crystallization of the perovskite layer^[44], while the MgF_2 ARC should induce a boost in the J_{sc} of around 0.7 mA/cm^2 .^[45] These optimizations resulted in a champion power conversion efficiency of 22.2% (23.8 mA/cm^2 , 1.12V, 83.5%), with negligible hysteresis (HI = 0.32).

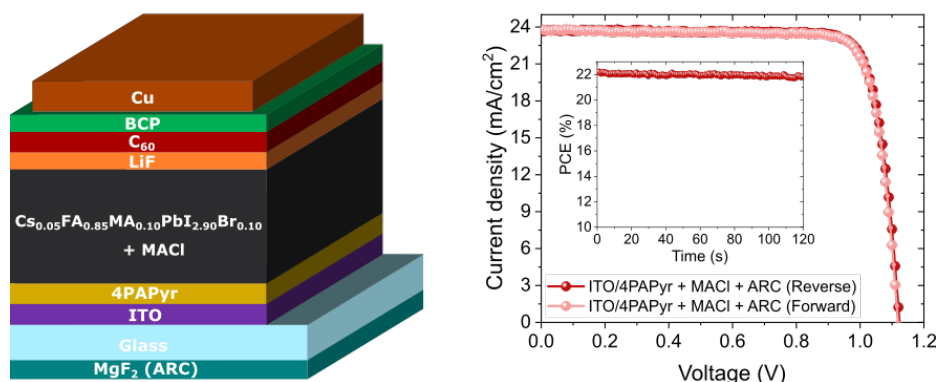


Figure 6: Schematic depiction of optimized device stack with 4PAPyr, MACl, and reflective coating (left), J-V curve of champion device with 22.2% PCE and MPPT stability as an inset (right).

It must be noted that the alkyl chain length of the novel SAMs has not been optimized. However, since we compare the performance of our novel SAMs to that of the carbazole reference SAM **2PACz**, for which the chain length has been optimized in the literature^[28], we can conclude that our novel pyrene-based SAM **4PAPyr** already outperforms the carbazole-based SAM without dedicated optimization of the chain length. It may well be that a pyrene-based SAM with a different chain length would result in additional performance enhancements.

Charge selectivity of SAMs

Transient surface photovoltage (trSPV) measurements were performed to compare the charge selectivity and injection capabilities of the **4PAPyr** and **2PACz** SAMs (Fig. 7). In trSPV measurements, a laser excites carriers in the perovskite layer of half devices (ITO/HTL/perovskite), which will then selectively migrate to the hole-transporting layer. The measured change in the surface potential on the top surface of the half device indicates how many and how efficiently holes are extracted from the perovskite layer to the underlying HTL.^[28]

The trSPV signal of **4PAPyr** exhibits a similar time to peak but with twice the intensity compared to **2PACz**, indicating that this SAM enables more efficient hole extraction. The comparable time to peak suggests that the primary advantage of **4PAPyr** lies in its enhanced hole selectivity, resulting in more net holes being transferred to ITO. This improvement is likely due to superior energetic alignment and/or better overall coverage of **4PAPyr**. Note that next to the coverage, it has been shown that also the molecular ordering of the phosphonic acids in the SAM can have an important influence on the charge transport.^[46]

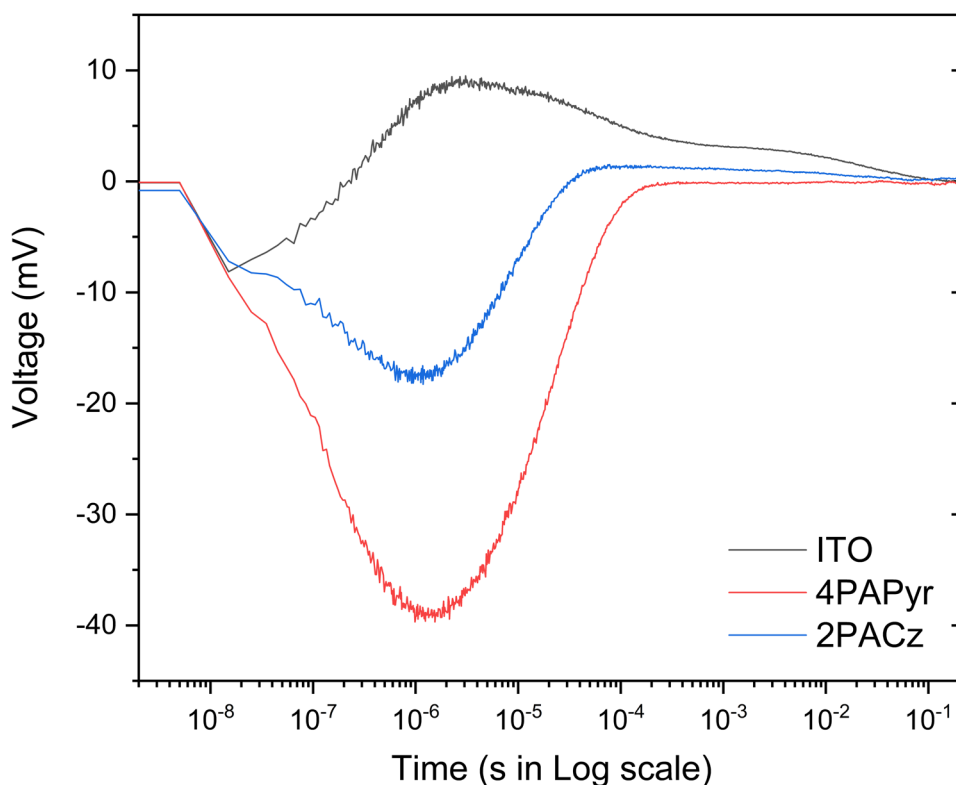


Figure 7: *tr*-SPV measurements of perovskite deposited on blank ITO (Black), 4PAPyr covered ITO (Red), and 2PACz covered ITO (Blue).

Relative coverage of the SAMs on ITO

To further examine the difference in coverage on ITO between **4PAPyr** and **2PACz**, CV measurements were performed on SAM-coated ITO substrates. By comparing the obtained cyclic voltammograms of SAM-coated ITO with the voltammogram obtained for bare ITO, the relative coverage of SAMs on ITO can be determined qualitatively.^[47] The peak separation between the oxidation and reduction peak (ΔE_p) in the voltammogram is dependent on the rate of electron transfer. Thus, ΔE_p provides a measure of how effective the respective SAMs are at blocking the access of redox species to the underlying ITO electrode and hence provides an indication of the extent of defects in the SAM. The higher the value of ΔE_p , the more hindered electron transfer is between the ITO and the redox species and, hence, the lower the number of defects in the SAM.

Figure 8 shows the CV curves of bare ITO and **4PAPyr** or **2PACz** covered ITO. The oxidation and reduction peak positions of **2PACz**-covered ITO (ΔE_p : 0.304V) are relatively close to those of bare ITO (ΔE_p : 0.236V), indicating the presence of defects in the SAM and thus an overall coverage that is quite poor. For **4PAPyr**-covered ITO, on the other hand, the oxidation and reduction peak positions are drastically shifted from those of bare ITO (ΔE_p : 0.781V), indicating that there are fewer defects in this SAM. These findings are in line with our device data, where

the yield (percentage of working devices) with **4PAPyr** was significantly higher than the yield of devices with **2PACz** as HTL.

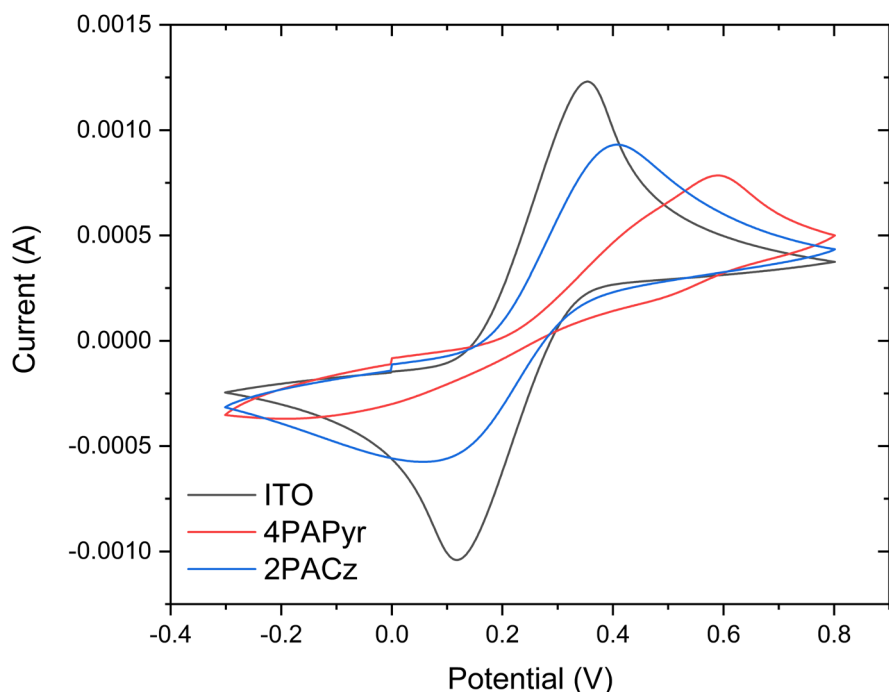


Figure 8: cyclic voltammograms of blank ITO (Black), 4PAPyr covered ITO (Red), and 2PACz covered ITO (Blue).

Additionally, AFM phase imaging was conducted on multiple **2PACz** and **4PAPyr** samples. This imaging technique effectively measures local compositional variations by leveraging material-specific elasticity. It helps to distinguish between two polymers in an organic blend^[48], or, as in this study, to identify areas with variable SAM coverage on ITO, such as pinholes^[49] or regions of reduced molecular density. The phase signal was collected concurrently with the 5x5 μm topographic images. Figure 9 (a,c) illustrates local dark spots where the phase signal significantly drops. The associated topographic images are shown in Figure 9 (b,d). In Figure 9c, **2PACz** exhibits a notably higher number of such spots, with a median area of 191 nm² and a total coverage of such spots of 2%. Conversely, the **4PAPyr** sample shows a spot coverage of less than 1%, with a median area of 95 nm². Figure 9e provides a closer view of local spots in the phase signal, with these features extending up to 50 nm in width, exemplified by the black arrow. The surface roughness is likely not contributing to the phase peak difference, as the RMS roughness for both **2PACz** and **4PAPyr** is comparable, at 2.5 nm and 2.8 nm, respectively.

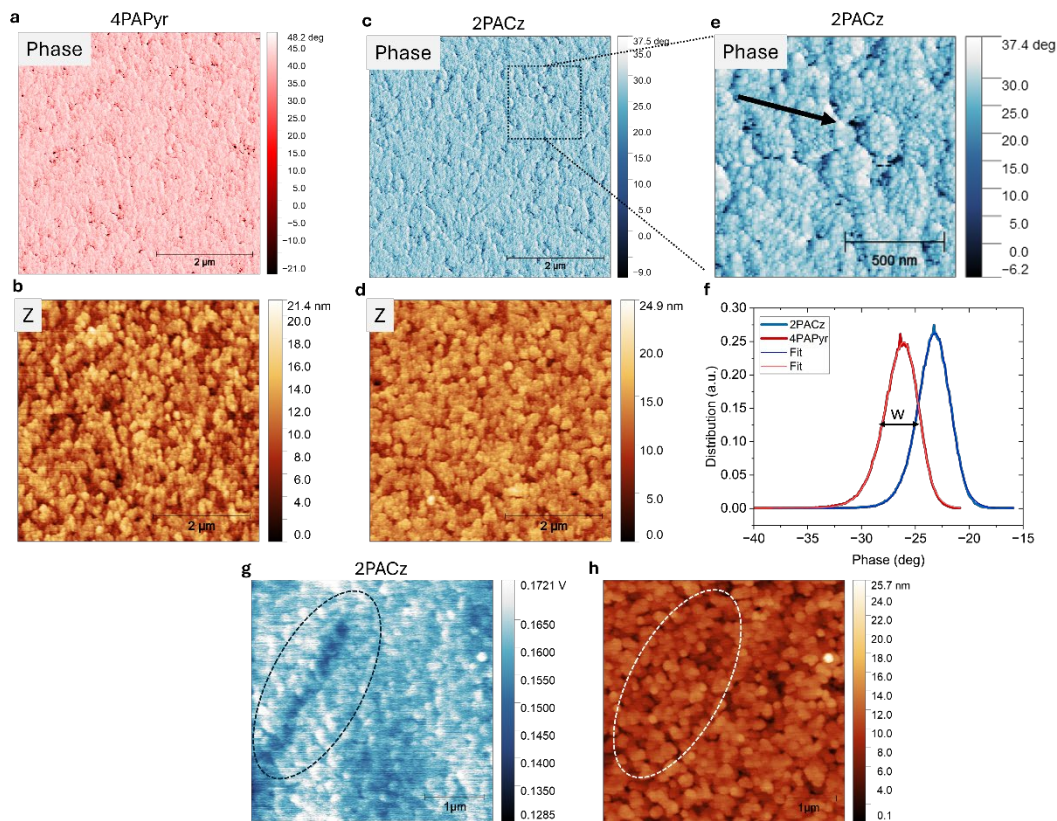


Figure 9: (a,c) Phase map of 4PAPyr and 2PACz. (b,d) Accompanied topographic image of a,c. (e) zoom-in of (c) showing local defects in the phase imaging of local pin holes. (f) Statistical phase distribution showing the full-width half maximum (W). (g) Local defect in the local CPD map of 2PACz. (h) The defect for which no correlation with the local morphology is observed.

Despite these differences in pinholes in certain local spots, variations in pinhole density are not constant over different samples for **2PACz**. A comparison of a new set of **2PACz** and **4PAPyr** samples revealed minimal statistical variation in the phase signal, as shown in Fig. 9f, with the full-width half maximum (W) differing by only 0.3° between the two SAMs. This suggests that, including the previous measurements, **2PACz** is locally able to cover ITO to a similar degree as **4PAPyr** but not consistently. Additional evidence of **2PACz**'s susceptibility to outlier behavior was obtained by measuring the contact potential difference (CPD) between the AFM tip and the surface with electrostatic force microscopy.^[50] The CPD, which often correlates with the work function^[51], is sensitive to differences in aggregation density and electronic inhomogeneities, especially in conductivity. Figure 9g presents an example where large CPD defects, spanning several micrometers, are noted in the CPD signal for **2PACz**. Such significant deviations are expected to adversely affect device performance with **2PACz**. These variations are not correlated to morphological changes, as indicated by the area within the dashed white line in Fig. 9h. No such large local deviations in the CPD map were observed on any of the measured **4PAPyr** samples. In summary, these microscopy measurements indicate that **4PAPyr** consistently results in a similar coverage on ITO while **2PACz** can occasionally locally cover ITO to a similar degree as **4PAPyr**, but is more prone to show larger area defects and is susceptible to sample-to-sample differences. These conclusions are in line with the CV measurements which are only sensitive to overall average coverage over an entire substrate.

Finally, the coverage of both SAMs was compared by performing contact angle measurements at several spots on samples of ITO covered with **4PAPyr** and **2PACz** respectively (Fig. S17). Table S3 shows that across all measurements **4PAPyr** has a slightly higher contact angle (θ_c) than **2PACz** with an average of 82.9° compared to 79.1°. This minor difference is not expected to result in important differences in wettability. More importantly, the standard deviation between different contact angle measurements on **4PAPyr** (0.2°) is ten times lower than that of measurements on **2PACz** (2.1°). This, together with the CV and AFM measurements, further confirms that the coverage of **4PAPyr** on ITO is much more uniform and consistent than that of **2PACz**, which in turn results in an overall higher yield of working devices for **4PAPyr**.

Conclusions

In this work, three new self-assembled monolayers (SAMs) have successfully been synthesized and incorporated as a hole-transporting layer (HTL) in *p-i-n* perovskite solar cells. While two of these SAMs were unsuitable as HTL due to a poor energy level alignment with the perovskite, the pyrene-based SAM **4PAPyr** exhibited superior energy level alignment and achieved promising device results, including a 22.2% power conversion efficiency for the champion device.

Furthermore, **4PAPyr** clearly outperformed the conventionally used carbazole-based SAM **2PACz**, not only in power conversion efficiency but also in film coverage, resulting in a significantly higher yield of working devices when spin-coating the SAM directly onto ITO. The improved coverage, compared to the commercially available SAM, could be particularly beneficial for larger modules, where poor coverage has a more pronounced impact on efficiency, opening a promising avenue for further research. Finally, devices with **4PAPyr** showed increased stability during 180 hours of MPPT, maintaining 93% of the initial efficiency after the burn-in period, compared to 74% for **2PACz**.

The presented results showcase the flexibility in the molecular design of SAMs as HTLs, allowing for the modulation of critical parameters such as energy level alignment and surface coverage to achieve reproducible and efficient perovskite solar cells.

Supporting Information

Supporting Information is available from the Wiley Online Library or from the authors.

Acknowledgments

The authors thank the Research Foundation – Flanders (FWO Vlaanderen) for continuous financial support. S.Le, S.La, A.K., T.A., L.L., D.V., and W.T.M.V.G. thank the FWO for the funding of the FWO-SBO project PROCEED (S002019N). L.L., D.V. and W.T.M.V.G. are grateful to the FWO for the funding of the senior FWO research projects G043320N and G0A8723N. T.C. is an FWO postdoctoral fellow (1284623N). M.V. acknowledges Eindhoven University of Technology for funding. This study was supported by the special research fund (BOF) of Hasselt University (BOF21GP04).

References

- [1] National Renewable Energy Laboratory, NREL, 2024.
- [2] a)T. Lemerrier, L. Perrin, E. Planès, S. Berson, L. Flandin, *Energies* **2020**, *13*, 3794; b)C. Momblona, L. Gil-Escrig, E. Bandiello, E. M. Hutter, M. Sessolo, K. Lederer, J. Blochwitz-Nimoth, H. J. Bolink, *Energy Environ. Sci.* **2016**, *9*, 3456.
- [3] a)X. Lin, D. Cui, X. Luo, C. Zhang, Q. Han, Y. Wang, L. Han, *Energy & Environmental Science* **2020**, *13*, 3823; b)S. Liu, V. P. Biju, Y. Qi, W. Chen, Z. Liu, *NPG Asia Materials* **2023**, *15*.
- [4] H. Zhang, N.-G. Park, *DeCarbon* **2024**, *3*, 100025.
- [5] Y. H. Wang, L. P. Duan, M. Zhang, Z. Hameiri, X. Liu, Y. Bai, X. J. Hao, *Solar Rrl* **2022**, *6*, 2200234.
- [6] J. You, L. Meng, T.-B. Song, T.-F. Guo, Y. Yang, W.-H. Chang, Z. Hong, H. Chen, H. Zhou, Q. Chen, Y. Liu, N. De Marco, Y. Yang, *Nature Nanotechnology* **2016**, *11*, 75.
- [7] M. Sendner, J. Trollmann, A. Pucci, *Organic Electronics* **2014**, *15*, 2959.
- [8] C. C. Boyd, R. C. Shallcross, T. Moot, R. Kerner, L. Bertoluzzi, A. Onno, S. Kavadiya, C. Chosy, E. J. Wolf, J. Werner, J. A. Raiford, C. de Paula, A. F. Palmstrom, Z. J. Yu, J. J. Berry, S. F. Bent, Z. C. Holman, J. M. Luther, E. L. Ratcliff, N. R. Armstrong, M. D. McGehee, *Joule* **2020**, *4*, 1759.
- [9] a)F. Ali, C. Roldán-Carmona, M. Sohail, M. K. Nazeeruddin, *Adv Energy Mater* **2020**, *10*, 2002989; b)S. Y. Kim, S. J. Cho, S. E. Byeon, X. He, H. J. Yoon, *Adv Energy Mater* **2020**, *10*, 2002606.
- [10] a)H. Bi, Y. Fujiwara, G. Kapil, D. Tavgeniene, Z. Zhang, L. Wang, C. Ding, S. R. Sahamir, A. K. Baranwal, Y. Sanehira, K. Takeshi, G. Shi, T. Bessho, H. Segawa, S. Grigalevicius, Q. Shen, S. Hayase, *Advanced Functional Materials* **2023**, *33*; b)A. R. M. Alghamdi, M. Yanagida, Y. Shirai, G. G. Andersson, K. Miyano, *ACS Omega* **2022**, *7*, 12147.
- [11] R. Guo, X. R. Zhang, X. Zheng, L. Li, M. Li, Y. Zhao, S. J. Zhang, L. Luo, S. You, W. X. Li, Z. M. Gong, R. Huang, Y. Cui, Y. G. Rong, H. P. Zeng, X. Li, *Advanced Functional Materials* **2023**, *33*, 2211955.
- [12] A. Al-Ashouri, E. Kohnen, B. Li, A. Magomedov, H. Hempel, P. Caprioglio, J. A. Marquez, A. B. Morales Vilches, E. Kasparavicius, J. A. Smith, N. Phung, D. Menzel, M. Grischek, L. Kegelmann, D. Skroblin, C. Gollwitzer, T. Malinauskas, M. Jost, G. Matic, B. Rech, R. Schlatmann, M. Topic, L. Korte, A. Abate, B. Stannowski, D. Neher, M. Stolterfoht, T. Unold, V. Getautis, S. Albrecht, *Science* **2020**, *370*, 1300.
- [13] M. Pitaro, J. E. S. Alonso, L. Di Mario, D. G. Romero, K. Tran, J. Kardula, T. Zaharia, M. B. Johansson, E. M. J. Johansson, R. C. Chiechi, M. A. Loi, *Advanced Functional Materials* **2023**.
- [14] E. J. Cassella, E. L. K. Spooner, T. Thornber, M. E. O'Kane, T. E. Catley, J. E. Bishop, J. A. Smith, O. S. Game, D. G. Lidzey, *Adv Sci (Weinh)* **2022**, *9*, e2104848.
- [15] A. Farag, T. Feeney, I. M. Hossain, F. Schackmar, P. Fassel, K. Küster, R. Bäuerle, M. A. Ruiz-Preciado, M. Hentschel, D. B. Ritzer, A. Diercks, Y. Li, B. A. Nejand, F. Laufer, R. Singh, U. Starke, U. W. Paetzold, *Adv Energy Mater* **2023**, *13*, 2203982.
- [16] a)Y. Yao, C. Cheng, C. Zhang, H. Hu, K. Wang, S. De Wolf, *Adv Mater* **2022**, *34*, e2203794; b)Z. Li, Q. Tan, G. Chen, H. Gao, J. Wang, X. Zhang, J. Xiu, W. Chen, Z. He, *Nanoscale* **2023**, *15*, 1676.
- [17] A. Al-Ashouri, A. Magomedov, M. Ross, M. Jost, M. Talaikis, G. Chistiakova, T. Bertram, J. A. Márquez, E. Köhnen, E. Kasparavicius, S. Levenco, L. Gil-Escrig, C. J. Hages, R. Schlatmann, B. Rech, T. Malinauskas, T. Unold, C. A. Kaufmann, L. Korte, G. Niaura, V. Getautis, S. Albrecht, *Energy & Environmental Science* **2019**, *12*, 3356.
- [18] W. Jiang, F. Li, M. Li, F. Qi, F. R. Lin, A. K. Jen, *Angew Chem Int Ed Engl* **2022**, *61*, e202213560.
- [19] a)A. Ullah, K. H. Park, H. D. Nguyen, Y. Siddique, S. F. A. Shah, H. Tran, S. Park, S. I. Lee, K. K. Lee, C. H. Han, K. Kim, S. Ahn, I. Jeong, Y. S. Park, S. Hong, *Adv Energy Mater* **2022**, *12*, 2103175; b)A. Ullah, K. H. Park, Y. Lee, S. Park, A. Bin Faheem, H. D. Nguyen, Y. Siddique, K. K. Lee, Y. Jo, C. H. Han, S. Ahn, I. Jeong, S. Cho, B. Kim, Y. S. Park, S. Hong, *Advanced Functional Materials* **2022**, *32*, 2208793.
- [20] a)A. Al-Ashouri, M. Marcinkas, E. Kasparavicius, T. Malinauskas, A. Palmstrom, V. Getautis, S. Albrecht, M. D. McGehee, A. Magomedov, *Acs Energy Letters* **2023**, *8*, 898; b)S. M. Park, M. Wei, N. Lempeis, W. Yu, T. Hossain, L. Agosta, V. Carnevali, H. R. Atapattu, P. Serles, F. T. Eickemeyer, H.

- Shin, M. Vafaie, D. Choi, K. Darabi, E. D. Jung, Y. Yang, D. B. Kim, S. M. Zakeeruddin, B. Chen, A. Amassian, T. Filleter, M. G. Kanatzidis, K. R. Graham, L. Xiao, U. Rothlisberger, M. Gratzel, E. H. Sargent, *Nature* **2023**, 624, 289.
- [21] S. L. Wang, D. Khan, W. C. Zhou, Y. J. Sui, T. Zhang, G. P. Yu, Y. M. Huang, X. Q. Yang, X. Q. Chen, H. Yan, J. Tang, F. Yang, P. G. Han, Z. L. Zheng, Y. Z. Zhang, Z. G. Tang, *Advanced Functional Materials* **2024**, 34, 2316202.
- [22] C. E. Puerto Galvis, D. A. Gonzalez Ruiz, E. Martinez-Ferrero, E. Palomares, *Chem Sci* **2024**, 15, 1534.
- [23] W. T. M. Van Gompel, R. Herckens, K. Van Hecke, B. Ruttens, J. D'Haen, L. Lutsen, D. Vanderzande, *ChemNanoMat* **2019**, 5, 323.
- [24] C. Niebel, Y. G. Kim, C. Ruzié, J. Karpinska, B. Chattopadhyay, G. Schweicher, A. Richard, V. Lemaire, Y. Olivier, J. Cornil, A. R. Kennedy, Y. Diao, W. Y. Lee, S. Mannsfeld, Z. N. Bao, Y. H. Geerts, *Journal of Materials Chemistry C* **2015**, 3, 674.
- [25] S. Lammar, W. Van Gompel, S. Lenaers, M. Mertens, H.-G. Boyen, D. Desta, A. Hadipour, L. Lutsen, D. Vanderzande, A. Krishna, Y. Abdulraheem, T. Aernouts, J. Poortmans, *Journal of Materials Chemistry C* **2023**, 11, 8146.
- [26] P. H. Denis, M. Mertens, W. T. M. Van Gompel, A. Maufort, S. Mertens, Z. M. Wei, M. Van Landeghem, S. Gielen, B. Ruttens, D. Deduytsche, C. Detarvernier, L. Lutsen, F. Grozema, K. Vandewal, D. Vanderzande, *Advanced Optical Materials* **2022**, 10, 2200788.
- [27] M. V. Khenkin, E. A. Katz, A. Abate, G. Bardizza, J. J. Berry, C. Brabec, F. Brunetti, V. Bulovic, Q. Burlingame, A. Di Carlo, R. Cheacharoen, Y. B. Cheng, A. Colmann, S. Cros, K. Domanski, M. Dusza, C. J. Fell, S. R. Forrest, Y. Galagan, D. Di Girolamo, M. Graetzel, A. Hagfeldt, E. von Hauff, H. Hoppe, J. Kettle, H. Koebler, M. S. Leite, S. Liu, Y. L. Loo, J. M. Luther, C. Q. Ma, M. Madsen, M. Manceau, M. Matheron, M. McGehee, R. Meitzner, M. K. Nazeeruddin, A. F. Nogueira, C. Odabasi, A. Osherov, N. G. Park, M. O. Reese, F. De Rossi, M. Saliba, U. S. Schubert, H. J. Snaith, S. D. Stranks, W. Tress, P. A. Troshin, V. Turkovic, S. Veenstra, I. Visoly-Fisher, A. Walsh, T. Watson, H. B. Xie, R. Yildirim, S. M. Zakeeruddin, K. Zhu, M. Lira-Cantu, *Nature Energy* **2020**, 5, 35.
- [28] I. Levine, A. Al-Ashouri, A. Musiienko, H. Hempel, A. Magomedov, A. Drevilkauskaitė, V. Getautis, D. Menzel, K. Hinrichs, T. Unold, S. Albrecht, T. Dittrich, *Joule* **2021**, 5, 2915.
- [29] E. A. Kraut, R. W. Grant, J. R. Waldrop, S. P. Kowalczyk, *Physical Review Letters* **1980**, 44, 1620.
- [30] a) P. Schulz, E. Edri, S. Kirmayer, G. Hodes, D. Cahen, A. Kahn, *Energy & Environmental Science* **2014**, 7, 1377; b) F. Y. Zhang, S. H. Silver, N. K. Noel, F. Ullrich, B. P. Rand, A. Kahn, *Adv Energy Mater* **2020**, 10, 1903252.
- [31] J. Endres, M. Kulbak, L. F. Zhao, B. P. Rand, D. Cahen, G. Hodes, A. Kahn, *Journal of Applied Physics* **2017**, 121, 035304.
- [32] a) H. Kang, S. J. Cho, G. D. Kong, S. Park, H. J. Yoon, *Surf Interfaces* **2022**, 34, 102401; b) H. Kang, S. J. Cho, G. D. Kong, H. J. Yoon, *Nano Lett* **2022**, 22, 4956; c) Y. B. Liu, S. Notz, H. R. Lang, M. Zharnikov, *J Phys Chem C* **2023**, 127, 19290.
- [33] A. Magomedov, A. Al-Ashouri, E. Kasparavicius, S. Strazdaite, G. Niaura, M. Jost, T. Malinauskas, S. Albrecht, V. Getautis, *Adv Energy Mater* **2018**, 8, 1801892.
- [34] a) J. J. Sun, C. H. Shou, J. S. Sun, X. L. Wang, Z. H. Yang, Y. Chen, J. R. Wu, W. C. Yang, H. L. Long, Z. Q. Ying, X. Yang, J. Sheng, B. J. Yan, J. C. Ye, *Solar Rrl* **2021**, 5; b) L. Mao, T. Yang, H. Zhang, J. Shi, Y. Hu, P. Zeng, F. Li, J. Gong, X. Fang, Y. Sun, X. Liu, J. Du, A. Han, L. Zhang, W. Liu, F. Meng, X. Cui, Z. Liu, M. Liu, *Adv Mater* **2022**, 34, e2206193; c) F. H. Isikgor, S. Zhumagali, L. V. T. Merino, M. De Bastiani, I. McCulloch, S. De Wolf, *Nat Rev Mater* **2023**, 8, 89; d) N. Phung, M. Verheijen, A. Todinova, K. Datta, M. Verhage, A. Al-Ashouri, H. Kobler, X. Li, A. Abate, S. Albrecht, M. Creatore, *ACS Appl Mater Interfaces* **2022**, 14, 2166.
- [35] R. Saive, *IEEE Journal of Photovoltaics* **2019**, 9, 1477.
- [36] B. Roose, K. Dey, Y. H. Chiang, R. H. Friend, S. D. Stranks, *J Phys Chem Lett* **2020**, 11, 6505.
- [37] Y. Gao, H. Raza, Z. P. Zhang, W. Chen, Z. H. Liu, *Advanced Functional Materials* **2023**, 33, 2215171.

- [38] X. P. Zheng, Z. Li, Y. Zhang, M. Chen, T. Liu, C. X. Xiao, D. P. Gao, J. B. Patel, D. Kuciauskas, A. Magomedov, R. A. Scheidt, X. M. Wang, S. P. Harvey, Z. H. Dai, C. L. Zhang, D. Morales, H. Pruetz, B. M. Wieliczka, A. R. Kirmani, N. P. Padture, K. R. Graham, Y. F. Yan, M. K. Nazeeruddin, M. D. McGehee, Z. L. Zhu, J. M. Luther, *Nature Energy* **2023**, *8*, 462.
- [39] L. Lin, L. Yang, G. Z. Du, X. F. Li, Y. N. Li, J. D. Deng, K. Wei, J. B. Zhang, *Acs Applied Energy Materials* **2023**, *6*, 10303.
- [40] J. Chen, D. Lee, N. G. Park, *ACS Appl Mater Interfaces* **2017**, *9*, 36338.
- [41] a)J. Liu, M. Y. Hu, Z. H. Dai, W. X. Que, N. P. Padture, Y. Y. Zhou, *Acs Energy Letters* **2021**, *6*, 1003; b)T. Zhang, S. H. Cheung, X. Meng, L. Zhu, Y. Bai, C. H. Y. Ho, S. Xiao, Q. Xue, S. K. So, S. Yang, *J Phys Chem Lett* **2017**, *8*, 5069; c)J. Herterich, M. Unmüssig, G. Loukeris, M. Kohlstädt, U. Würfel, *Energy Technology* **2021**, *9*, 2001104.
- [42] a)C. H. Peters, I. T. Sachs-Quintana, W. R. Mateker, T. Heumueller, J. Rivnay, R. Noriega, Z. M. Beiley, E. T. Hoke, A. Salleo, M. D. McGehee, *Adv Mater* **2012**, *24*, 663; b)W. R. Mateker, M. D. McGehee, *Adv Mater* **2017**, *29*, 1603940.
- [43] Y. A. Olanrewaju, K. Orisekeh, O. V. Oyelade, R. K. Koech, R. Ichwani, A. I. Ebunu, D. I. Amune, A. Bello, V. C. Anye, O. K. Oyewole, W. O. Soboyejo, *Aip Advances* **2022**, *12*.
- [44] F. Zheng, C. Zuo, M. Niu, C. Zhou, S. J. Bradley, C. R. Hall, W. Xu, X. Wen, X. Hao, M. Gao, T. A. Smith, K. P. Ghiggino, *ACS Applied Materials & Interfaces* **2020**, *12*, 25980.
- [45] L. J. Xu, J. Liu, F. Toniolo, M. De Bastiani, M. Babics, W. B. Yan, F. Z. Xu, J. X. Kang, T. Allen, A. Razzaq, E. Aydin, S. De Wolf, *Acs Energy Letters* **2022**, *7*, 2370.
- [46] a)E. A. Weiss, R. C. Chiechi, G. K. Kaufman, J. K. Kriebel, Z. Li, M. Duati, M. A. Rampi, G. M. Whitesides, *J Am Chem Soc* **2007**, *129*, 4336; b)G. D. Kong, M. Kim, S. J. Cho, H. J. Yoon, *Angew Chem Int Ed Engl* **2016**, *55*, 10307; c)L. Jiang, L. Yuan, L. Cao, C. A. Nijhuis, *J Am Chem Soc* **2014**, *136*, 1982.
- [47] X. Chen, E. Luis, N. Darwish, S. Ciampi, P. Thordarson, J. J. Gooding, *Langmuir* **2012**, *28*, 9487.
- [48] E. Werner, U. Güth, B. Brockhagen, C. Döpke, A. Ehrmann, *Technologies* **2023**, *11*, 56.
- [49] S. Manzo, P. J. Strohbeen, Z. H. Lim, V. Saraswat, D. Du, S. Xu, N. Pokharel, L. J. Mawst, M. S. Arnold, J. K. Kawasaki, *Nat Commun* **2022**, *13*, 4014.
- [50] S. Howell, D. Kuila, B. Kasibhatla, C. P. Kubiak, D. Janes, R. Reifenberger, *Langmuir* **2002**, *18*, 5120.
- [51] S. Sadewasser, C. Barth, *Characterization of Materials* **2012**, *1*.